Journal of the Indian Chemical Society 101 (2024) 101335

Contents lists available at ScienceDirect

Journal of the Indian Chemical Society

journal homepage: www.journals.elsevier.com/journal-of-the-indian-chemical-society

Synthesis and characterization of nickel-based MOFs: Enhancing photocatalysis and targeted cancer drug delivery

A.H. Hatin Betseba [a,b], Y. Christabel Shaji [a,b,*], Y. Brucely [c,**], K. Sakthipandi [d,***]

[a] Department of Chemistry, Holy Cross College (Autonomous), Nagercoil, Tamil Nadu, India
[b] Affiliated to Manonmaniam Sundaranar University, Tirunelveli, India
[c] Department of Mechanical Engineering, SRM TRP Engineering College, Tiruchirappalli, 621 105, Tamil Nadu, India
[d] Department of Physics, SRM TRP Engineering College, Tiruchirappalli, 621 105, Tamil Nadu, India

ARTICLE INFO

Keywords:
Ni-based MOFs
Teflon autoclave
Hydrothermal method
MDA-MB-231

ABSTRACT

Metal–organic frameworks (MOFs) are intricate molecular solids formed by connecting organic ligands with metal or metal–cluster binding sites. They have exceptional characteristics such as expansive surface area, adaptability, and meticulously structured porosity, rendering them valuable in various applications including photocatalytic degradation and drug delivery systems. In this investigation, a benign Ni-based MOF was synthesized using benzene 1,4dicarboxylic acid as a linker and dimethyl sulfoxide as a solvent through the hydrothermal approach within a Teflon autoclave. The synthesized MOFs were precisely characterized using techniques such as X-ray diffraction, scanning electron microscope with energy-dispersive X-ray analysis, Fourier-transform infrared (FTIR) spectroscopy, thermogravimetric analysis, and N_2-sorption measurements. The photocatalytic efficiency of the Ni-based MOF was explored against Congo red under visible light exposure, with the proposed mechanism involving electron transfer from photoexcited organic ligands to metallic clusters, resulting in a degradation efficiency of 98.68 % after 145 min. Furthermore, the Ni-based MOFs, when loaded with the anticancer drug cisplatin, displayed notable capabilities in drug delivery against the human breast cancer cell line MDA-MB-231, leading to a 35.26 % reduction in cell viability. Cytotoxicity assessments using the MTT assay revealed that the nano-carriers hindered cell proliferation with an IC_{50} value of 46.84 μg/mL.

1. Introduction

Metal–organic frameworks (MOFs) have attracted significant attention in recent decades for their versatile nature and customizable crystalline structures, comprising metal ions or clusters interconnected by organic ligands via coordination bonds [1–7]. With remarkable attributes such as extensive surface area, adaptable metal sites, robust mechanical and thermal stability, tunable pore characteristics, and structural diversity, MOFs have found applications across catalysis [3], gas storage [4], biomedicine [5], substance separation [6], and nanomaterials [7]. Various synthesis methods, including solvothermal, hydrothermal, microwave-assisted, and mechanochemical approaches, offer advantages in scalability, reproducibility, and control over particle properties [8]. This article delves into two promising arenas where MOFs demonstrate exceptional performance: photocatalytic dye degradation and advanced drug delivery systems, reflecting their versatility in environmental remediation and healthcare innovation [9]. The escalating industrialization and urbanization have imperiled water bodies globally, with over 10,000 tons of dyes discharged annually, posing a significant environmental hazard [10]. Wastewater contamination, exacerbated by heavy metal ions, pigments, and organic pollutants, necessitates effective remediation strategies [11]. In the MTT assay, the Cis@Ni-based MOF exhibited concentration-dependent effects on MDA-MB-231 cells, with the data presented in Table 1 detailing the percentage of growth inhibition and cellular viability across various concentrations (μg/ml).

Efforts to develop effective photocatalysts for visible light applications have led to the advancement of various techniques, including electrolysis, oxidation, catalytic reduction, membrane separation, and photocatalytic degradation, aiming at dye removal [12].

* Corresponding author. Department of Chemistry, Holy Cross College (Autonomous), Nagercoil, Tamil Nadu, India.
** Corresponding author.
*** Corresponding author.
E-mail addresses: shajichristabel@gmail.com (Y. Christabel Shaji), brucely2k6@gmail.com (Y. Brucely), sakthipandi@gmail.com (K. Sakthipandi).

https://doi.org/10.1016/j.jics.2024.101335
Received 13 June 2024; Received in revised form 15 August 2024; Accepted 19 August 2024
Available online 22 August 2024

Table 1
MTT assay of Cis@Ni-based MOF on MDA-MB-231.

Concentrations (μg/ml)	% of cellular viability	% of growth inhibition
6.25	88.34	11.66
12.5	74.79	25.21
25	58.94	41.06
50	46.29	53.71
100	35.26	64.71

Semiconductors such as TiO_2, metal oxides [13], and metal sulfides serve as efficient photocatalysts for dye breakdown and decolorization [14]. Water-soluble dyes, known for their vibrant colors, pose significant environmental risks due to their resistance to biodegradation and chemical stability, often leading to adverse effects on human health and aquatic life [15–18]. MOFs have emerged as promising adsorbent materials for hazardous substance removal, leveraging their unique ability to catalyze the photodegradation of organic dyes [19].

MOFs offer distinct advantages over zeolites in catalytic applications, as they do not require high-temperature activation or regeneration [20,21]. Their semiconductor behavior in under light exposure and ability to separate charges make them versatile for applications such as solar fuel production, photovoltaics, and photocatalytic transformations [22–26]. Dye contamination in water bodies, particularly by azo dyes, poses significant environmental risks, which are exacerbated by their resistance to traditional removal methods [27–32]. Photocatalytic degradation emerges as an effective, eco-friendly solution, with materials such as UiO-66(Ti) and TiO_2 encapsulated in NH_2-MIL-101(Cr) demonstrating high efficiency in dye degradation [33–38]. Cancer, a leading cause of mortality worldwide, has prompted the exploration of innovative treatment strategies [39]. Chemotherapy, while improving survival rates, presents adverse side effects and lacks selectivity [40]. MOFs have gained attention in biomedicine, particularly for drug delivery, owing to their nano-scale size and biocompatibility [41,42]. Nano-MOFs hold promise for targeted drug delivery and controlled release, offering potential applications in various medical fields [43–46]. Notably, IRMOF-3 demonstrates efficacy in delivering curcumin to treat triple-negative breast cancer cells [47–50]. MOFs' well-defined structures and coordination bonds further enhance their suitability for drug delivery and cancer treatment [51]. The novel Ni(BDC)-MOF demonstrated exceptional catalytic performance for CR degradation, achieving 98.68 % efficiency within 145 min without H_2O_2, due to its high superoxide radical generation. Additionally, the cisplatin-infused Ni-based MOF exhibited a 35.26 % reduction in cell viability against MDA-MB-231 cells in MTT assays, selectively targeting cancer cells without harming normal L-929 cells.

This study aimed to investigate the catalytic activity of the novel Ni-based MOF in the photocatalytic degradation of Congo red under ambient conditions. The choice of Ni-based MOF was driven by its promising electronic and photocatalytic properties, as well as its unique structural characteristics. Congo red served as a model molecule to evaluate the photocatalytic capabilities of the Ni-based MOF. Additionally, this study proposed a preliminary design for a smart drug delivery system using the novel Ni-based MOF features for active targeting of cisplatin to triple-negative breast cancer MDA-MB-231 cell lines. By using the Ni-based MOF as a carrier for loaded cisplatin, our primary objective was to develop effective nano-drugs for breast cancer treatment and assess their efficacy using the 3-[4,5-dimethylthiazol-2-yl]-2,5-diphenyl tetrazolium bromide (MTT) assay.

2. Materials and methods

2.1. Synthesis of Ni-based MOFs

Nickel chloride hexahydrate, benzene 1,4 dicarboxylic acid, dimethyl sulfoxide (DMSO), cisplatin, and Congo red were procured from Sigma-Aldrich without further purification. The MDA-MB-231 cell line was obtained from the National Centre for Cell Sciences (NCCS), Pune, India. Ni-based MOF synthesis was conducted via a hydrothermal method in a Teflon autoclave. Nickel chloride hexahydrate (0.0145 mmol) was dissolved in 20 mL deionized water whereas benzene 1,4 dicarboxylic acid (BDC) (0.18 mmol) was dissolved in 20 mL DMSO. The resulting transparent solutions were mixed and heated at 180 °C for 12 h. After cooling, the precipitate was collected by centrifugation, washed three times, and dried at 150 °C.

2.2. Loading of cisplatin in Ni-based MOF

Cisplatin loading in the Ni-based MOF involved immersing 300 mg MOF in a cisplatin solution and stirring at room temperature for 72 h. After centrifugation to remove the solvent, the MOF was dried in an oven for 4 h at 80 °C to eliminate water molecules before cisplatin loading. The percentage of drug loading capacity was calculated by subtracting the weight of the drug-loaded MOF from the weight of the MOF alone, and dividing this difference by the weight of the MOF.

2.3. Characterization

To characterize the Ni-based MOF, the following characterizations were used. X-ray diffraction (XRD) analysis using a Bruker binary V4 X-ray diffractometer was conducted to assess phase purity and crystal structure, with Cu Kα irradiation spanning a range of 10°–80°. The Quanta FEG-250 SEM instrument was used to investigate particle morphology, coupled with composition analysis via energy-dispersive X-ray microanalysis. The Brunauer–Emmett–Teller (BET) surface area of the prepared samples was determined through N_2 adsorption–desorption isotherm analysis using a QuantaChrome NOVA-1200. Functional groups were identified using the Shimadzu IR Affinity-1 Fourier transform infrared (FTIR) spectrometer over a wavenumber range of 4000–400 cm^{-1}. UV–vis spectroscopy was performed using the UV-1800 series with a light source wavelength of 340 nm, whereas X-ray photoelectron spectroscopy (XPS) was conducted using the Phi VersaProbe III.

2.4. Photocatalytic degradation of Congo red dye

In this study, the role of the MOF as a photocatalyst to degrade Congo red dye was examined. The process involved the use of a light source, typically UV–vis light, to energize the electrons within the MOF, creating electron–hole pairs that aid in breaking down the dye molecules. To conduct the photocatalytic experiment, a solution containing approximately 0.001 g (1 ppm) Congo red dye dissolved in 1000 mL double-distilled water was prepared. Subsequently, about 0.005 g of the catalyst was added to 40 mL of the dye solution. The mixture was then thoroughly stirred in darkness to ensure even dispersion of the dye within the photocatalyst suspension. Following this step, the reaction vessel containing the photocatalyst solution was positioned under the light source to ensure consistent illumination. The experiment commenced, with the initial time ($t = 0$) recorded. At regular intervals (0, 15, 30, 45, 60, 75, 90, 120, and 145 min), samples were collected, each comprising approximately 4 mL from the reaction mixture. These samples were later analyzed using UV–vis spectroscopy to monitor the degradation of the dye over time.

2.5. Cell culture and maintenance

For cell culture and maintenance, Dulbecco's modified Eagle's medium (DMEM; HiMedia) was used and supplemented with 10 % heat-inactivated fetal bovine serum and a 1 % antibiotic cocktail consisting of penicillin (100 U/ml), streptomycin (100 μg/mL), and amphotericin B (2.5 μg/mL). The cells were cultured in tissue culture (TC) flasks (25 cm^2), which were then placed in a cell culture incubator set at 37 °C with

5 % CO_2 and humidity.

2.6. Cytotoxicity test by MTT assay

To evaluate the cytotoxicity of test samples, the MTT assay was conducted. Initially, cells (2500 cells/well) were seeded onto 96-well plates and allowed to acclimatize to the culture conditions for 24 h. Test samples, prepared in DMEM media (10 mg/mL), were filter-sterilized and further diluted in DMEM media to achieve final concentrations ranging from 6.25 to 100 μg/mL. Untreated wells were maintained as controls. All experiments were performed in triplicate to ensure accuracy. After a 24-h incubation period, the media from the wells were aspirated, and 100 μL of 0.5 mg/mL MTT solution in phosphate-buffered saline (PBS) was added to each well. Following a 2-h incubation, the formazan crystals formed were solubilized using DMSO, and the absorbance was measured to assess cell viability.

3. Results and discussion

The XRD analysis of the Ni-based MOF was conducted using Cu Kα radiation with a wavelength of 1.5406 Å. The crystal phase of the Ni-based MOF was accurately examined over a diffraction angle (2θ) range spanning from 10° to 80°. As depicted in Fig. 1(a), the XRD spectra exhibited distinctive features/peaks characteristic of the Ni-MOF, showcasing high-intensity diffraction peaks at $2\theta = 17.416°$, 27.975°, and 48.276°, corresponding to the crystallographic planes of (002), (024), and (102), respectively. Additionally, lower intensity peaks were observed at $2\theta = 25.179°$ and 41.269°, corresponding to the planes of (020) and (101). Notably, the most prominent peak for the Ni-based MOF was identified at $2\theta = 28.06$, indicating its crystalline nature with well-defined crystallographic patterns. To quantify the crystallite size, the Scherrer's equation was used:

$$D = \frac{k\lambda}{\beta \cos\theta}$$

Here, D represents the crystallite size, k is the Scherrer's constant (0.98), λ is the wavelength of the X-ray source (1.5406 Å), β is the full-width half maximum measured in radians on the 2θ scale, and θ is the Bragg angle for the diffraction peak. Using this equation, the average size of the Ni-based MOF was determined to be 42.044 nm, underscoring its well-defined crystalline structure. The characterization provided crucial insights into the structural properties of the Ni-based MOF, essential for understanding its potential applications in various fields.

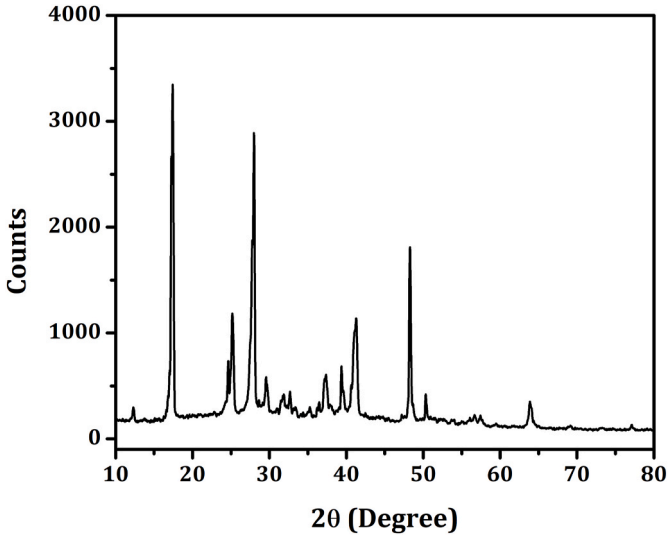

Fig. 1. XRD pattern of Ni-based MOF.

Similar findings were observed in the Omkaramurthy et al. study [52], which focused on Zn-based MOFs. The research confirmed the crystalline nature of Zn-MOFs and demonstrated effective coordination between the metal ions and organic ligands. The high crystallinity and phase purity of these MOFs are critical for their performance in applications such as catalysis, gas storage, and drug delivery, where structural precision and stability are paramount. The results from this investigation further corroborate the potential of MOF as versatile and robust materials for advanced technological applications [52].

The investigation into the size, shape, and elemental composition of the experimental sample involved the use of scanning electron microscopy (SEM) coupled with energy-dispersive X-ray analysis (EDAX). On analysis of SEM images in conjunction with EDAX data for the synthesized Ni-based MOF, distinct findings emerged. The SEM images revealed the presence of particles and bulk particles showing irregular structures, which spontaneously organized into aggregated clusters of particles (as depicted in Fig. 2), with an average diameter ranging from 1 to 40 μm. This observation underscores the successful synthesis of the Ni-based MOF, showcasing its predominance in fine forms and diverse morphology. Furthermore, the EDAX analysis facilitated chemical characterization and elemental analysis of the catalyst. Each energy peak detected in the spectrum corresponds to specific elements present in the sample. Notably, the EDAX spectrum of the synthesized Ni-based MOF showed the presence of elements such as Ni, C, O, and S, further confirming the structural composition of the MOF [53]. The combined SEM-EDAX analysis provides comprehensive insights into the structural properties and elemental composition of the synthesized Ni-based MOF, laying the groundwork for its potential applications in various fields ranging from catalysis to materials science.

Fig. 3 illustrates the FTIR spectra obtained for all synthesized MOFs. In Fig. 3(a), the absorption band observed at 3423.56 cm^{-1} corresponds to the symmetric and asymmetric stretching vibrations of the N–H group, whereas the band at 1632.78 cm^{-1} signifies the symmetric and asymmetric stretching vibrations of the H–N–H group [54]. In Fig. 3(b), the absorption band spanning from 3400 to 2500 cm^{-1} signifies the robust O–H stretching vibrations characteristic of the –COOH group. The supplementary absorption features at 2855.58, 2665.62, and 2547.97 cm^{-1} are attributed to overtones and absorption combinations within the intermolecular environment of BDC. The absorption peak observed at 3068.75 cm^{-1} corresponds to the aromatic C–H stretching vibration originating from BDC. Furthermore, a weak absorption band at 1673.28 cm^{-1} corresponds to the C═O stretching vibration from the carbonyl group of BDC whereas the band at 1518.35 cm^{-1} signifies the C═C stretching vibration from the aromatic ring. The absorption band at 1421.54 cm^{-1} corresponds to the symmetric stretching vibration of the CO group in the carboxylate, and the band at 1286.25 cm^{-1} indicates the stretching vibration of the C–O bond in the carboxylic acid group. Furthermore, the band observed at 674 cm^{-1} corresponds to the bending vibration of the aromatic ring in and out of the plane. Moreover, the distinct separation between symmetric and asymmetric stretching modes of the coordinated –COO group confirms the coordination of the –COO group of BDC to Ni^{2+}, further elucidating the structural composition of the synthesized MOFs [55].

The optical properties of the synthesized Ni-based MOF were examined using UV–vis diffuse reflectance spectroscopy, as illustrated in Fig. 4. In Fig. 4(a), the UV–vis absorption bands of the Ni-based MOF are observed to fall within the range of 250–350 nm. Remarkably, upon the deposition of Congo red dyes onto the Ni-based MOF, there is a discernible increase in the absorption intensities of Congo red @Ni-based MOF. This augmentation implies that within the Ni-based MOF, there is an enhanced generation of charge carriers (e^-/h^+) during the photocatalytic process, thereby amplifying its efficacy in degrading organic pollutants. Similarly, the absorption intensity of Cis@Ni-based MOF diminishes subsequent to the encapsulation of cisplatin, as depicted in Fig. 4(b) [56,57]. This reduction in absorption intensity suggests the successful incorporation of cisplatin within the Ni-based MOF

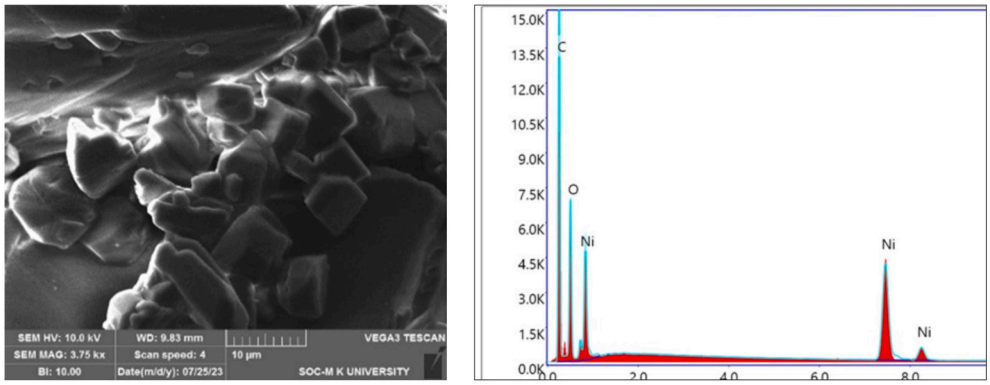

Fig. 2. SEM image and EDAX spectrum of Ni-based MOF.

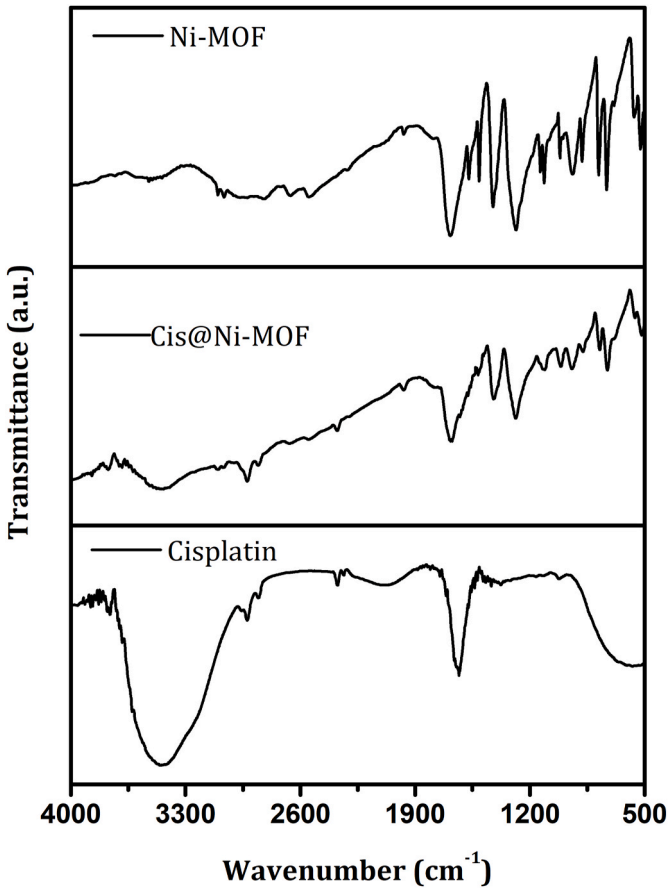

Fig. 3. FT-IR spectra of **a)** Cisplatin **b)**Ni-based MOF **c)** Cis@Ni-based MOF.

structure, thereby altering its optical characteristics. The optical bandgap energy refers to the energy needed to move electrons from the valence band to the conduction band. To convert reflectance to absorbance in UV–visible diffuse reflectance spectra, this energy was calculated using the Kubelka–Munk method:

$$\frac{K}{S} = \frac{(1-R)^2}{2R}$$

where K represents the molar absorption coefficient, S denotes the scattering factor, and R indicates the reflectance. It was found that the band gap for Ni-MOF was 3.61 eV. These findings highlight how material composition and encapsulation affect the optical properties of the synthesized materials, revealing their potential applications in optical and photocatalytic processes.

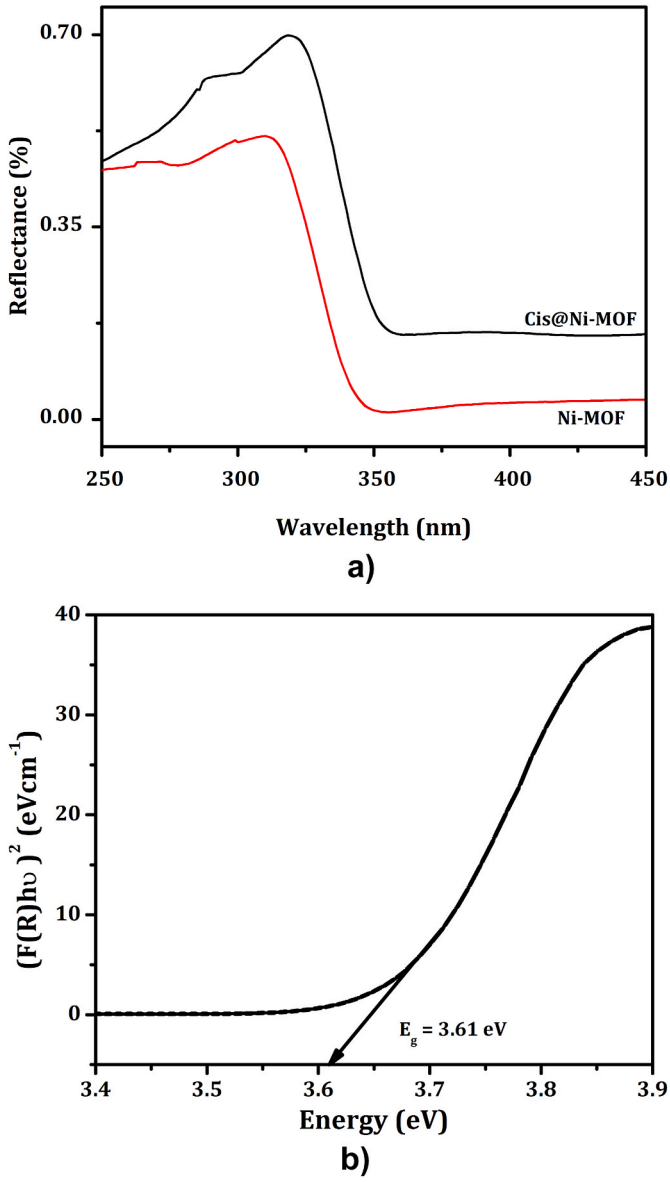

Fig. 4. UV-DRS of **a)** Ni-based MOF and **b)** Cis@Ni-based MOF.

To investigate into the elemental chemical states, XPS technique was used. Fig. 5 shows the XPS spectrum, revealing the chemical states of key components Ni, C, O, and S within the Ni-based MOF. In the survey

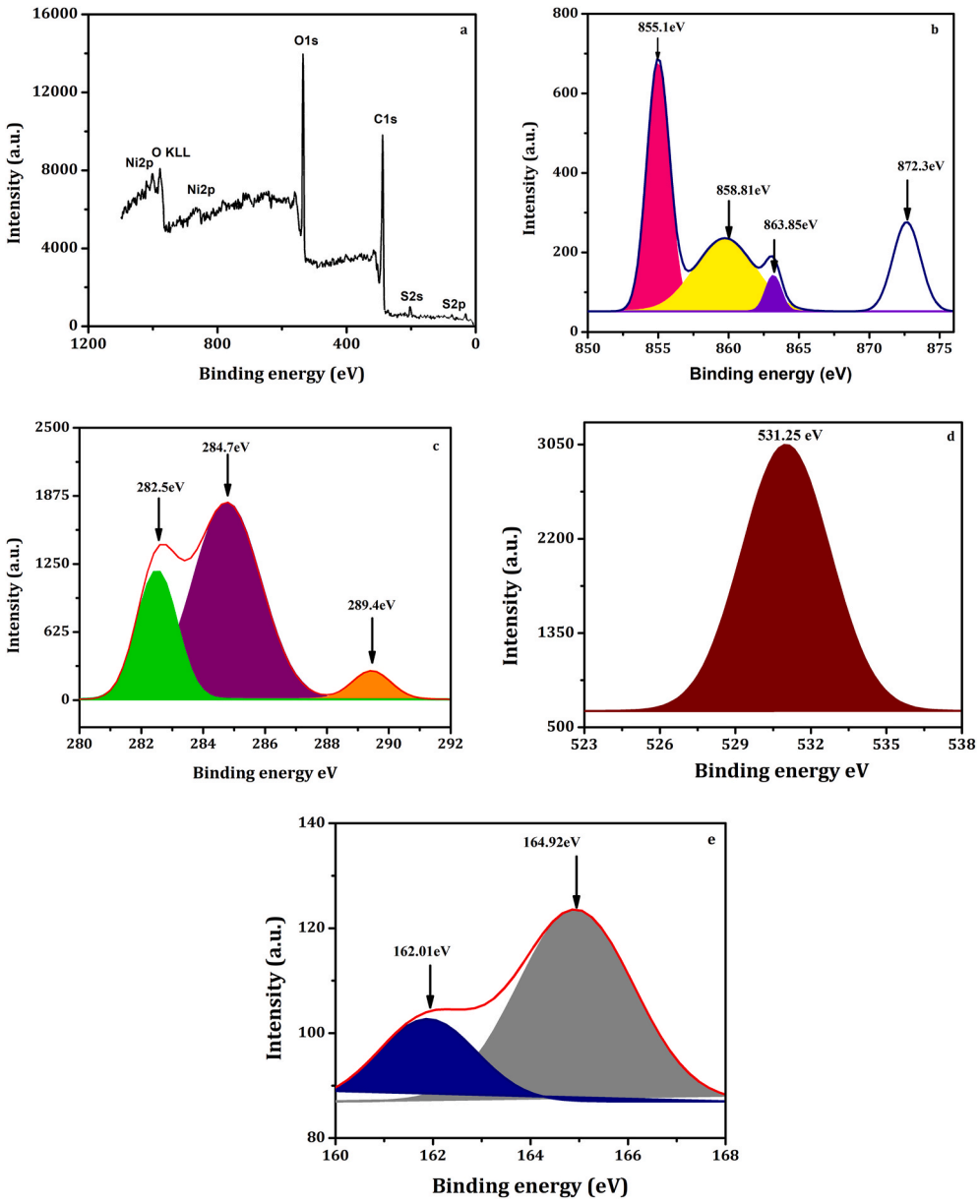

Fig. 5. XPS of **a)** Ni-based MOF **b)** Ni2p **c)** C1s **d)** O1s **e)** S2p.

spectrum (Fig. 5(a)), distinct peaks corresponding to Ni 2p, C1s, O1s, and S2p were observed, confirming their presence. Notably, Fig. 5(b) illustrates closely spaced Ni *2p* peaks at 855.1 and 872.3 eV, attributed to Ni^{2+} $2p_{3/2}$ and $2p_{1/2}$ states, respectively. Weak satellite peaks at approximately 863.85–858.81 eV are assigned to normal Ni-MOFs, as per previous analyses. The C1s peak at 282.5, 284.7, and 289.4 eV correspond to the C═C, C–C, and C═O of carbonyl groups and O1s peaks at 531.25 eV correspond to the –OH group, respectively (Fig. 5(c & d)). Furthermore, *S2p* peaks were observed around 164.92 eV (Fig. 5 (e)). These findings suggest a consistent structure across the as-prepared Ni-MOFs, although variations in morphology are evident [58].

Thermogravimetric analysis (TGA) was conducted to assess the thermal stability of both Ni- and Cis@Ni-based MOF. In Fig. 6(a), TGA of Ni-based MOF reveals four distinct mass drops. The initial drop of 5.33 % occurred between room temperature and 231 °C, attributed to desorption of surface water and organic solvents. Subsequently, at 257 and 321 °C, mass drops of 23.43 % and 29.78 % were observed, indicating potential decomposition in the skeletal structure. The final drop of 19.04 % was noted between 333 and 415 °C. Above 415 °C, the mass remained stable, with less than 25 % residue, suggesting thermal stability up to 310 °C in open air. In Fig. 6(b), TGA of Cis@Ni-based MOF shows five mass drops. The initial drop of 3.2 % occurred at 73 °C, followed by drops of 9.3 % and 39.05 % at 192 and 306 °C, respectively. Additional drops of 5.38 % and 16.32 % were observed between 300 and 455 °C. Similar to the Ni-based MOF, residue remained below 30 % above 455 °C. Thermal stability was determined to be below 270 °C in open air. Notably, the Ni-based MOF demonstrated higher thermal stability compared to the Cis@Ni-based MOF [59].

The porosity of a drug delivery system significantly influences its effectiveness. To assess the porosity, BET and Barrett–Joyner–Halenda techniques were used to determine specific surface area, pore volume, pore diameters, and isotherm types of the synthesized MOFs. Nitrogen sorption measurements were conducted at 77 K for all materials. According to BET analysis, the Ni-based MOF exhibited a surface area of 441.22 m^2/g, a total pore volume of 0.054 cm^3/g, and a mean pore diameter of 1.923 nm. Conversely, the cisplatin-loaded Ni-based MOF showed slightly reduced values: a surface area of 364.53 m^2/g, a total pore volume of 0.031 cm^3/g, and a mean pore diameter of 1.523 nm.

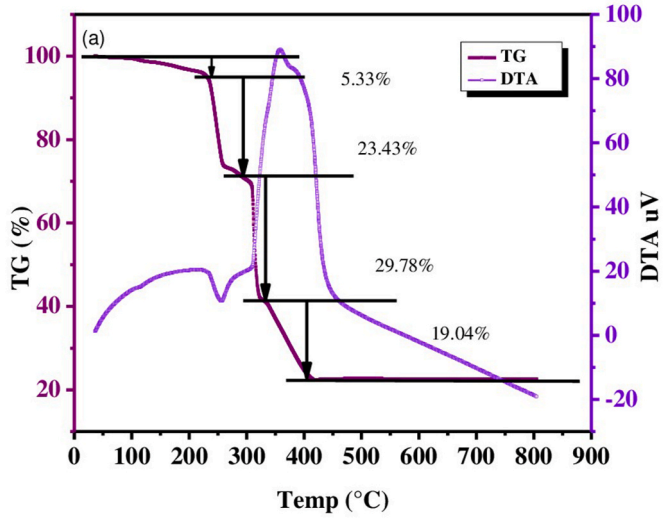

(a)

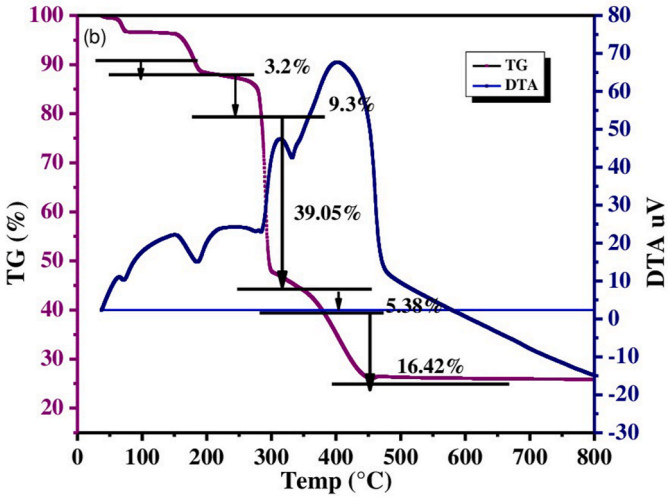

(b)

Fig. 6. TGA of (a)Ni-based MOF (b)Cis@Ni-based MOF

This reduction in pore size in Cis@Ni-based MOF indicates efficient loading of cisplatin within the MOF structure, enhancing drug encapsulation compared to Ni-based MOF alone [60,61]. Hoai et al. [60] reported a notable reduction in the pore size and pore volume of MIL-53 upon incorporating polyethylene glycol. Specifically, the pore size decreased from 31 to 7.22 nm, and the pore volume diminished from 0.213 to 0.072 cm^3/g. These reductions confirm the successful encapsulation of PEG within the MIL-53 framework [62]. Similarly, Siamak et al. [63] observed a significant decrease in the surface area of Cu-MOF from 1260 to 920.15 m^2/g following the loading of Ibuprofen (IBU). This decrease in surface area and porosity indicates the effective incorporation of IBU into the Cu-MOF structure, suggesting reduced accessibility of the internal pore network post-encapsulation [63]. These studies highlight the impact of guest molecule incorporation on the structural properties of MOF.

In the absence of the Ni-based MOF catalyst, the UV–vis spectra of Congo red dye exhibited a peak at 499 nm. Upon the addition of 0.005 g of the Ni-based MOF catalyst, the UV–vis spectra showed a decrease in the λ_{max} value corresponding to the 499 nm peak, with no emergence of additional peaks at various time intervals. The peaks associated with Congo red dye gradually diminished over time, indicating the ongoing degradation of the dye. The degradation process was carried out for up to 145 min under UV–vis light until complete dye degradation occurred and the same is shown in Fig. 7. Castellanos et al. [64] reported a remarkable achievement in the photocatalytic degradation of CR using titanium-based MOFs. Their study demonstrated a substantial degradation efficiency of 96 % after just 3 h of irradiation. Furthermore, the researchers introduced a novel nickel-based MOF, which exhibited an even more impressive degradation performance. This new MOF achieved a 97 % degradation of CR in only 145 min, outperforming the titanium-based MOF in both efficiency and speed [64]. The remarkable performance of the Ni-based MOF can be attributed to its unique catalytic properties, including heightened light absorption and efficient charge separation capabilities. This underscores the photocatalytic activity of the Ni-based MOF, highlighting its potential as an effective and environmentally sustainable solution for removing Congo red dye from aqueous solutions. To quantify the degradation of Congo red, the percentage of degradation was calculated using the formula:

$$\%\ \text{of the degradation} = \frac{A_0 - A_t}{A_0} \times 100$$

where A_0 represents the absorbance at time $t = 0$, and A_t represents the absorbance after a given treatment time t. Both A_0 and A_t are measured at the λ_{max} of the dye.

The mechanism underlying the photocatalytic degradation of CR dye can be comprehensively understood through the lens of semiconductor theory, as elucidated by prior research. Central to this process is the phenomenon of ligand-to-metal charge transfer, where electrons are transferred from the photoexcited organic ligand to the metal ions within MOFs [61]. In the synthesis of Ni-based MOFs, the coordination of Ni ions with BDC ligands plays a pivotal role. This coordination leads to the formation of a porous architecture within the MOFs, which presents potential active sites for catalysis, particularly on exposure to UV–vis light.

On illumination, the catalysts absorb photons, causing electrons to transition from the valence band to the conduction band, consequently generating electron–hole pairs (e^- and h^+). These photo-induced electrons migrate to the conduction band, whereas the resulting holes remain in the valence band of the MOF catalysts. Subsequently, the holes react with water molecules to form hydroxyl radicals ($^{\bullet}OH$). The Congo red molecules, adsorbed onto the surface of the catalyst through interactions with metal sites and organic linkers, are then attacked by

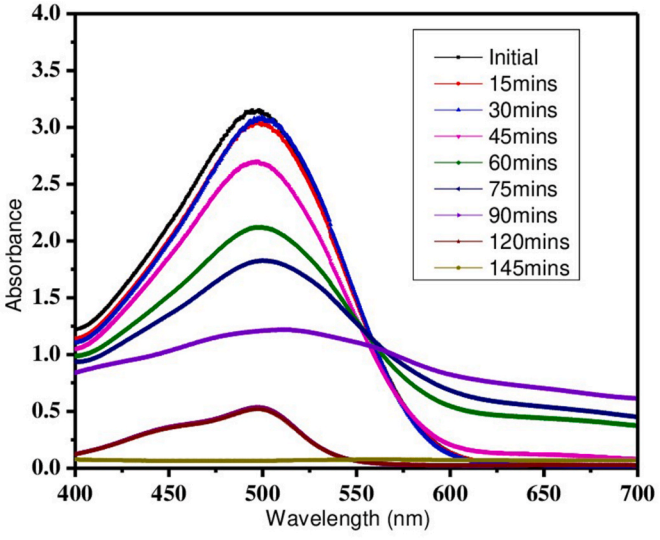

Fig. 7. UV–vis spectrum of Ni-based MOF.

these hydroxyl radicals. Meanwhile, the electrons in the conduction band engage in a reaction with molecular oxygen, yielding superoxide radicals ($^{\bullet}O^{2-}$), which in turn react with the adsorbed Congo red. Throughout the photocatalytic process, the superoxide radicals ($^{\bullet}O^{2-}$) and holes (h^{+}) participate actively in redox reactions with Congo red molecules, leading to the degradation of the dye into smaller and less toxic by-products. This intricate interplay of electron transfer, radical formation, and redox reactions underscores the efficacy of Ni-based MOFs as catalysts for the degradation of Congo red dye.

$$NiCl_2 + BDC \rightarrow Ni(BDC)$$

$$Ni\ (BDC) + h\upsilon \rightarrow \left(Ni^{2+}BDC\right) * + e^{-} + h^{+}$$

$$h^{+} + H_2O \rightarrow {}^{\bullet}OH + h+$$

$$^{\bullet}OH + \text{Congo red dye} \rightarrow \text{Degradation product}$$

$$\widehat{e}(-) + O\_(2) \rightarrow \dot{(\bullet)}\ O\_(2)\widehat{\ }(-$$

$$\text{Adsorbed Congo red} + {}^{\bullet}O_2^{-} \rightarrow \text{Degradation products.}$$

The cytotoxicity of cisplatin-loaded Ni-based MOF was evaluated through an MTT assay, which assessed cellular viability by measuring mitochondrial function. Initially, a 96-well plate containing MDA-MB-231 cells, both viable and nonviable, was cultured and incubated individually for 24 h. Subsequently, the MDA-MB-231 cells were exposed to incremental twofold dilutions of Cis@Ni-MOF to evaluate its antiproliferative effect. MTT solution, reconstituted in PBS, was then added to the wells containing Cis@Ni-MOF-treated cells and untreated control wells. Following incubation in a humidified environment at 37 °C with 5 % CO_2, the active mitochondria in viable cells cleaved the tetrazolium ring in MTT, producing insoluble formazan crystals, a process exclusive to living cells. The purple formazan crystals were solubilized in DMSO, serving as a solvent. After removing the supernatant liquid, the dissolved formazan crystals were quantified spectrophotometrically at 570 nm. The absorbance of the formazan solution correlates with the total number of viable cells. The percentage of cellular viability was calculated from triplicate measurements at various concentrations using the formula:

$$\%\ \text{of cellular viability} = \frac{\text{Average absorbance of treated}}{\text{Average absorbance of control}} \times 100$$

The assessment of the cytotoxic effects of cisplatin-loaded Ni-based MOF was carried out on two distinct cell lines: MDA-MB-231, a breast cancer cell line, and L-929, a normal mouse fibroblast cell line. After a 24-h incubation period of both MDA-MB-231 and L-6 cell cultures, test samples with concentrations ranging from 6.25 to 100 μg/mL were administered to the cultured cells, with untreated cells serving as controls. On addition of MTT dye to the cultured 96-well plates containing MDA-MB-231 cells treated with Cis@Ni-MOF, a discernible purple color change was observed. This color change was attributed to the presence of the chelating ligand, electron-withdrawing group of the tricarboxylate ligand, and cisplatin incorporated in Cis@Ni-MOF, facilitating the targeted delivery of cisplatin specifically to the cancer cell line while sparing the normal cell line from damage.

Initially, when MDA-MB-231 cells were exposed to 6.25 μg/ml Cis@Ni-based MOF, the cell viability percentage was measured at 88.34 %. However, as the concentration increased to 12.5 μg/mL, the viability percentage decreased to 74.79 %. Further escalations to concentrations of 25, 50, and 100 μg/mL resulted in viability percentages of 58.94, 46.29, and 35.26, respectively. Notably, cellular viability decreased with increasing concentrations of Cis@Cu-based MOF, longer degradation times, and extended incubation periods, although relatively favorable viability rates were observed at higher concentrations (up to 100 μg/mL). At higher doses and longer incubation periods, viability decreased more rapidly. Fig. 8 presents the cell image of breast cancer MDA-MB-231, demonstrating a decrease in cell viability with increasing concentration. Siamak et al. [65] reported on a copper-based MOF (Cu-MOF) loaded with ibuprofen and tested its effects on Caco-2 cells. The study found that when exposed to Cu-MOF/IBU@GM, Caco-2 cells exhibited no cytotoxicity and maintained a 60 % survival rate. In contrast, both Cu-MOF and IBU/Cu-MOF, unlike Cu-MOF/IBU@GM, caused significant harm to Caco-2 cells even at low concentrations [65]. Further, a nickel-based MOF loaded with cisplatin demonstrated a viability of 35.26 % against MDA-MB-231 cells, indicating that Ni-based MOFs are more biocompatible than Cu-based MOFs loaded with ibuprofen. This suggests the potential of Ni-based MOFs as effective anticancer drug carriers. The graphical representation of concentration in μg/mL versus cellular viability percentage is depicted in Fig. 9.

Chen et al. [66] reported the incorporation of 3-MA into ZIF-8 and assessed cellular viability using an MTT assay. After a 24-h treatment with 3-MA@ZIF-8 NPs at a concentration of 7.5 μg/mL (equivalent to 1.5 μg/mL 3-MA), mitochondrial function in HeLa cells decreased to 60 % of the initial level. When treated with 10 μg/mL 3-MA@ZIF-8 NPs, mitochondrial function dropped significantly to below 10 % [66]. Liang et al. [67] evaluated the cytotoxicity of BSA/DOX@ZIF on MCF-7 cells using an MTT assay. Following a 24-h treatment with BSA/DOX@ZIF at concentrations of 0.5 and 1 mg/L, mitochondrial function in MCF-7 cells decreased to 33 % and 17 % of the baseline level, respectively. Additionally, after a 72-h treatment with BSA/DOX@ZIF at a dosage of 1 mg/L, mitochondrial function in MCF-7 cells further decreased to approximately 10 %. The combined effects of BSA/DOX and ZIF resulted in the increased cytotoxicity of BSA/DOX@ZIF [67]. The Ni-based MOFs, loaded with 28.33 % cisplatin, functioned as effective drug carriers, facilitating enhanced cellular uptake of cisplatin, increasing its concentration within cancer cells and eliciting a more potent anticancer response. Moreover, as the concentration increased, the percentage of growth inhibition rose from 11.66 % to 64.71 %. These results suggest that increasing the concentration of the complex led to a decrease in the percentage viability of the MDA-MB-231 cell line. The IC_{50} value for the antiproliferative activity of Cis@Ni-MOF on MDA-MB-231 was determined to be 46.84 μg/mL, indicative of its promising anticancer efficacy.

4. Conclusion

The synthesis and application of innovative MOFs with new topologies and functionalities have significantly advanced in recent years. This study reports the synthesis of a nontoxic Ni-based MOF via the hydrothermal method and its characterization. The photocatalytic activity of the Ni-based MOF was evaluated by degrading Congo red dye in an aqueous solution under visible light irradiation, achieving a degradation rate of up to 98.75 % after 145 min under optimal conditions, demonstrating its potential for wastewater treatment. Further, the in vitro anticancer efficacy of cisplatin-loaded Ni-based MOFs was tested on MDA-MB-231 breast cancer cells using the MTT assay, reducing cell viability to 35.26 % at a concentration of 100 μg/mL, with an IC50 value of 46.84 μg/mL. These results highlight the promising applications of MOFs in photocatalysis and drug delivery, paving the way for further research in sustainable chemistry, nanomedicine, and environmental science.

CRediT authorship contribution statement

A.H. Hatin Betseba: Writing – original draft, Validation, Resources, Investigation, Data curation, Conceptualization. **Y. Christabel Shaji:** Writing – original draft, Resources, Project administration, Data curation, Conceptualization. **Y. Brucely:** Writing – review & editing, Validation, Project administration, Investigation. **K. Sakthipandi:** Writing – review & editing, Project administration, Formal analysis.

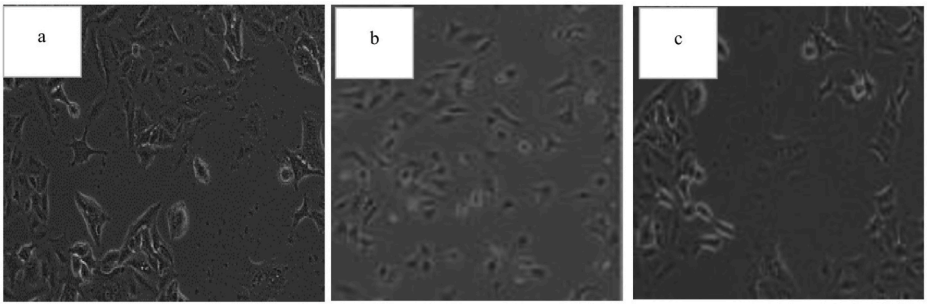

Fig. 8. MDA-MB-231 cell line treated with various concentrations **a)** 25 μg/ml **b)** 50 μg/mL **c)** 100 μg/mL of Cis@Ni-based MOF.

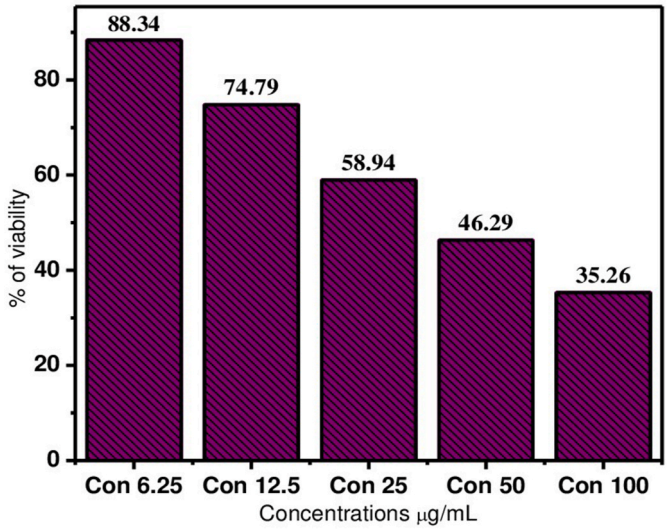

Fig. 9. Graphical representation of concentrations vs % of viability.

Declaration of competing interest

None.

The authors declare that they have no known competing financial interests or personal relationships that could have appeared to influence the work reported in this paper.

References

[1] R. Udaya Rajesh, T. Mathew, H. Kumar, A. Singhal, L. Thomas, Metal-organic frameworks: recent advances in synthesis strategies and applications, Inorg. Chem. Commun. 162 (2024) 112223, https://doi.org/10.1016/j.inoche.2024.112223.

[2] K.Y. Zou, Z.X. Li, Controllable syntheses of MOF-derived materials, Chem. Eur J. (2018), https://doi.org/10.1002/chem.201705415.

[3] R. Nivetha, P. Kollu, K. Chandar, S. Pitchaimuthu, S.K. Jeong, A.N. Grace, Role of MIL-53(Fe)/hydrated-dehydrated MOF catalyst for electrochemical hydrogen evolution reaction (HER) in alkaline medium and photocatalysis, RSC Adv. 9 (2019) 3215–3223, https://doi.org/10.1039/c8ra08208a.

[4] D. Kim, G. Lee, S. Oh, M. Oh, Unbalanced MOF-on-MOF growth for the production of a lopsided core-shell of MIL-88B@MIL-88A with mismatched cell parameters, Chem. Commun. 55 (2019) 43–46, https://doi.org/10.1039/c8cc08456d.

[5] C. Doonan, R. Ricco, K. Liang, D. Bradshaw, P. Falcaro, Metal-organic frameworks at the bio interface: synthetic strategies and applications, Acc. Chem. Res. 50 (2017) 1423–1432, https://doi.org/10.1021/acs.accounts.7b00090.

[6] S. Lin, Y. Zhao, Y.S. Yun, Highly effective removal of nonsteroidal anti-inflammatory pharmaceuticals from water by Zr(IV)-Based metal-organic framework: adsorption performance and mechanisms, ACS Appl. Mater. Interfaces 10 (2018) 28076–28085, https://doi.org/10.1021/acsami.8b08596.

[7] S. Hermes, F. Schroder, R. Chelmowski, C. Woll, R.A. Fischer, Selective nucleation and growth of metal-organic open framework thin films on patterned COOH/CF3-terminated self-assembled monolayers on Au (111), J. Am. Chem. Soc. 127 (2005) 13744–13745, https://doi.org/10.1021/ja053523l.

[8] Norbert Stock, Shyam Biswas, Synthesis of metal-organic frameworks (MOFs): routes to various MOF topologies, Morphologies, and Composites 112 (2) (2012) 933–969, https://doi.org/10.1021/cr200304e.

[9] A. Saravanan, P.S. Kumar, P.R. Yaashikaa, S. Karishma, S. Jeevanantham, S. Swetha, Mixed biosorbent of agro waste and bacterial biomass for the separation of Pb (II) ions from water system, Chemosphere 277 (2021) 130236, https://doi.org/10.1016/j.chemosphere.2021.130236.

[10] M.T. Yagub, T.K. Sen, S. Afroze, H.M. Ang, Dye and its removal from aqueous solution by adsorption: a review, Adv. Colloid Interface Sci. 209 (2014) 172–184, https://doi.org/10.1016/j.cis.2014.04.002.

[11] Q. Ma, Y. Li, Y. Tan, B. Xu, J. Cai, Y. Zhang, Q. Wang, Q. Wu, B. Yang, J. Huang, Recent advances in metal-organic framework (MOF)-Based photocatalysts: design strategies and applications in heavy metal control, Molecules 28 (18) (2022) 6681, https://doi.org/10.3390/molecules28186681.

[12] S. Saha, G. Das, J. Thote, R. Banerjee, Photocatalytic metal-organic framework from CdS quantum dot incubated luminescent metallohydrogel, J. Am. Chem. Soc. 136 (42) (2014) 14845–14851, https://doi.org/10.1021/ja509019k.

[13] Krzysztof Piaskowski, Renata Swiderska-Dabrowska, Paweł K. Zarzycki, Dye removal from water and wastewater using various physical, chemical, and biological processes, J. AOAC Int. 101 (5) (2018) 1371–1384, https://doi.org/10.5740/jaoacint.18-0051.

[14] M. Sharma, T. Jain, S. Singh, O. Pandey, Photocatalytic degradation of organic dyes under UV-visible light using capped ZnS nanoparticles, Sol. Energy 86 (1) (2011) 626–633, https://doi.org/10.1016/j.solener.2011.11.006.

[15] M. Asgher, H.N. Bhatti, Evaluation of thermodynamics and effect of chemical treatments on sorption potential of Citrus waste biomass for removal of anionic dyes from aqueous solutions, Ecol. Eng. 38 (2012) 79–85, https://doi.org/10.1016/J.ECOLENG.2011.10.004.

[16] A.A. Renita, K.H. Vardhan, P.S. Kumar, P.T. Ngueagni, A. Abilarasu, S. Nath, P. Kumari, R. Saravanan, Effective removal of malachite green dye from aqueous solution in hybrid system utilizing agricultural waste as particle electrodes, Chemosphere 273 (2021) 129634, https://doi.org/10.1016/j.chemosphere.2021.129634.

[17] K. Kadirvelu, M. Kavipriya, C. Karthika, M. Radhika, N. Vennilamani, S. Pattabhi, Utilization of various agricultural wastes for activated carbon preparation and application for the removal of dyes and metal ions from aqueous solutions, Bioresour. Technol. 87 (1) (2003) 129–132, https://doi.org/10.1016/s0960-8524(02)00201-8.

[18] N. Tara, S.I. Siddiqui, G. Rathi, S.A. Chaudhry, A.M. Inamuddin Asiri, Nano-engineered adsorbent for the removal of dyes from water: a review, Curr. Anal. Chem. 16 (2019) 14–40, https://doi.org/10.2174/1573411015666190117124344.

[19] Q. Meng, X. Xin, L. Zhang, F. Dai, R. Wang, D. Sun, A multifunctional Eu MOF as a fluorescent pH sensor and exhibiting highly solvent-dependent adsorption and degradation of rhodamine B, J. Mater. Chem. A 3 (2015) 24016–24021, https://doi.org/10.1039/C5TA04989J.

[20] F. Wang, C. Wang, Z. Yu, Two multifunctional Mn(II) metal-organic frameworks: synthesis, structures and applications as photocatalysis and luminescent sensor, Polyhedron 105 (2016) 49–55, https://doi.org/10.1016/j.poly.2015.11.043.

[21] A.U. Czaja, N. Trukhan, U. Muller, Industrial applications of metal-organic frameworks, Chem. Soc. Rev. 38 (2009) 1284.

[22] M. Alvaro, E. Carbonell, B. Ferrer, Semiconductor behavior of a metal-organic framework (MOF), Chem. Eur J. 13 (2007) 5106–5112, https://doi.org/10.1002/chem.200601003.

[23] R. Passalacqua, S. Perathoner, G. Centi, Semiconductor, molecular and hybrid systems for photoelectrochemical solar fuel production, J. Energy Chem. 26 (2017) 219–240, https://doi.org/10.1016/j.jechem.2017.03.004.

[24] P. Kumar, K. Vellingiri, K.H. Kim, Modern progress in metal-organic frameworks and their composites for diverse applications, Microporous Mesoporous Mater. 253 (2017) 251–265, https://doi.org/10.1016/j.micromeso.2017.07.003.

[25] Y. Su, Z. Zhang, H. Liu, Y. Wang, Cd_2Zn_8S@UiO-66-NH_2 nanocomposites as efficient and stable visible-light driven photocatalyst for H2 evolution and CO_2 reduction, Appl. Catal. B Environ. 200 (2017) 448–457, https://doi.org/10.1016/j.apcatb.2016.07.032.

[26] J.W. Cui, S.X. Hou, Y.H. Li, G.H. Cui, A multifunctional Ni(ii) coordination polymer: synthesis, crystal structure and applications as a luminescent sensor, electrochemical probe, and photocatalyst, Dalton Trans. 46 (2017) 16911–16924, https://doi.org/10.1039/C7DT03874G.

[27] T. Lazar, Color chemistry: synthesis, properties, and applications of organic dyes and pigments, 3rd revised edition, Color Res. Appl. 30 (2005) 313–314, https://doi.org/10.1002/col.20132.

[28] D. Rawat, V. Mishra, R.S. Sharma, Detoxification of azo dyes in the context of environmental processes, Chemosphere 155 (2016) 591–605, https://doi.org/10.1016/J.CHEMOSPHERE.2016.04.068.
[29] R.D. Saini, Textile organic dyes: polluting effects and elimination methods from textile wastewater, Int. J. Chem. Eng. Res. 9 (2017) 975–6442.
[30] B.J. Bruschweiler, C. Merlot, Azo dyes in clothing textiles can be cleaved into a series of mutagenic aromatic amines which are not regulated yet, Regul. Toxicol. Pharmacol. 88 (2017) 214–226, https://doi.org/10.1016/J.YRTPH.2017.06.012.
[31] E.A. Moawed, H.A. Kiwaan, M.M. Elshazly, Application of polyurethane@ Salvadora persica composite for detection and removal of acidic and basic dyes from wastewater, J. Taiwan Inst. Chem. Eng. 80 (2017) 894–900, https://doi.org/10.1016/j.jtice.2017.07.028.
[32] S.P. Keerthana, R. Yuvakkumar, P.S. Kumar, G. Ravi, D.V.N. Vo, D. Velauthapillai, Influence of tin (Sn) doping on Co3O4 for enhanced photocatalytic dye degradation, Chemosphere 277 (2021) 130325, https://doi.org/10.1016/j.chemosphere.2021.130325.
[33] S. Sharma, A. Bhattacharya, Drinking water contamination and treatment techniques, Appl. Water Sci. 7 (2017) 1043–1067, https://doi.org/10.1007/s13201-016-0455-7.
[34] S. Bolisetty, M. Peydayesh, R. Mezzenga, Sustainable technologies for water purification from heavy metals: review and analysis, Chem. Soc. Rev. 48 (2019) 463–487, https://doi.org/10.1039/C8CS00493E.
[35] L.H. Zhang, Y. Zhu, B.R. Lei, Y. Li, W. Zhu, Q. Li, Trichromatic dyes sensitized hkust-1 (MOF-199) as scavenger towards reactive blue 13 via visible-light photodegradation, Inorg. Chem. Commun. 94 (2018) 27–33, https://doi.org/10.1016/j.inoche.2018.05.027.
[36] S. Dhaka, R. Kumar, A. Deep, M.B. Kurade, S.W. Ji, B.H. Jeon, Metal-organic frameworks (MOFs) for the removal of emerging contaminants from aquatic environments, Coord. Chem. Rev. 380 (2019) 330–352, https://doi.org/10.1016/j.ccr.2018.10.003.
[37] A. Wang, Y. Zhou, Z. Wang, M. Chen, L. Sun, X. Liu, Titanium incorporated with UIO-66 (Zr)-type metal-organic framework (MOF) for photocatalytic application, RSC Adv. 6 (2016) 3671–3679, https://doi.org/10.1039/C5RA24135A.
[38] X. Li, Y. Pi, Q. Xia, Z. Li, J. Xiao, TiO_2 encapsulated in salicylaldehyde-NH_2-MIL-101 (Cr) for enhanced visible light-driven photodegradation of MB, Appl. Catal., B 191 (2016) 192–201, https://doi.org/10.1016/j.apcatb.2016.03.034.
[39] M. Garcia, A. Jemal, E.M. Ward, M.M. Center, Y. Hao, R.L. Siegel, M.J. Thun, Global Cancer Facts & Figures, American Cancer Society, Atlanta, GA, USA, 2007.
[40] S. Senapati, A.K. Mahanta, S. Kumar, P. Maiti, Controlled drug delivery vehicles for cancer treatment and their performance, Signal Transduct. Targeted Ther. 3 (2018) 7, https://doi.org/10.1038/s41392-017-0004-3.
[41] X. Dai, L. Xiang, T. Li, Z. Bai, Cancer hallmarks, biomarkers and breast cancer molecular subtypes, J. Cancer 7 (2016) 1281–1294, https://doi.org/10.7150/jca.13141.
[42] L. Zhidong, F. Shuran, G. Chuying, L. Weicong, C. Jinxiang, L. Baohong, L. Jianqiang, Metal-organic framework (MOF)- based nanomaterials for biomedical applications, Curr. Med. Chem. 26 (2019) 3341–3369, https://doi.org/10.2174/0929867325666180214123500.
[43] D. Mao, F. Hu Kenry, S. Ji, W. Wu, D. Ding, D. Kong, B. Liu, Metal-organic-framework-assisted in vivo bacterial metabolic labeling and precise antibacterial therapy, Adv. Mater. 30 (2018) 1706831, https://doi.org/10.1002/adma.201706831.
[44] Y. Chen, P. Li, J.A. Modica, R.J. Drout, O.K. Farha, Acid resistant mesoporous metal-organic framework toward oral insulin delivery: protein encapsulation, protection, and release, J. Am. Chem. Soc. 140 (2018) 5678–5681, https://doi.org/10.1021/jacs.8b02089.
[45] D.F. Sava Gallis, K.S. Butler, J.O. Agola, C.J. Pearce, A.A. McBride, Antibacterial countermeasures via metal-organic framework-supported sustained therapeutic release, ACS Appl. Mater. Interfaces 11 (2019) 7782–7791, https://doi.org/10.1021/acsami.8b21698.
[46] J. Gandara-Loe, I. Ortuno-Lizaran, L. Fernandez-Sanchez, J.L. Alio, N. Cuenca, A. Vega-Estrada, J. Silvestre-Albero, Metal-organic frameworks as drug delivery platforms for ocular therapeutics, ACS Appl. Mater. Interfaces 11 (2019) 1924–1931, https://doi.org/10.1021/acsami.8b20222.
[47] M. Ibrahim, R. Sabouni, G.A. Husseini, Anti-cancer drug delivery using metal-organic frameworks (MOFs), Curr. Med. Chem. 24 (2017) 193–214, https://doi.org/10.2174/0929867323666160926151216.
[48] H. Zhang, W. Jiang, R. Liu, J. Zhang, D. Zhang, Z. Li, Rational design of metal-organic framework nanocarrier-based codelivery system of doxorubicin hydrochloride/verapamil hydrochloride for overcoming multidrug resistance with efficient targeted cancer therapy, ACS Appl. Mater. Interfaces 9 (2017) 19687–19697, https://doi.org/10.1021/acsami.7b05142.
[49] J. Gordon, H. Kazemian, S. Rohani, MIL-53(Fe), MIL-101, and SBA-15 porous materials: potential platforms for drug delivery, Mater. Sci. Eng. C Mater 47 (2015) 172–179, https://doi.org/10.1016/j.msec.2014.11.046.
[50] R. Paulmurugan, R. Bhethanabotla, K. Mishra, K, Folate receptor-targeted polymeric micellar nanocarriers for delivery of orlistat as a repurposed drug against triple-negative breast cancer, Mol. Cancer Therapeut. 15 (2016) 221–231, https://doi.org/10.1158/1535-7163.
[51] R. Anand, F. Borghi, F. Manoli, I. Manet, V. Agostoni, P. Reschiglian, R. Gref, S. Monti, Host-guest interactions in Fe(III)-Trimesate MOF nanoparticles loaded with doxorubicin, J. Phys. Chem. B 118 (2014) 8532–8539, https://doi.org/10.1021/jp503809w.
[52] B. Omkaramurthy, G. Krishnamurthy, N. Prasad, Two new Zn (II) bdc Metal-Organic Frameworks based on benzene 1, 4-dicarboxylic acid: synthesis, Crystal structures, Luminescent properties and Electrochemical studies, Mater. Today: Proc. 22 (2019) 2179–2190, https://doi.org/10.1016/j.matpr.2020.03.298.
[53] Gilang Gumilar, Yusuf Kaneti, Joel Henzie, Sauvik Chatterjee, Jongbeom Na, Brian Yuliarto, Nugraha Nugraha, Aep Patah, Asim Bhaumik, Yusuke Yamauchi, General synthesis of hierarchical sheet/plate-like M-BDC (M = Cu, Mn, Ni, and Zr) metal-organic frameworks for electrochemical non-enzymatic glucose sensing, Chem. Sci. 11 (14) (2020) 3644–3655, https://doi.org/10.1039/C9SC05636J.
[54] M. Ghaferi, S. Amari, B.V. Mohrir, A. Raza, H.E. Shahmabadi, S.E. Alavi, Preparation, characterization, and evaluation of cisplatin-loaded polybutylcyanoacrylate nanoparticles with improved in vitro and in vivo anticancer activities, Pharmaceuticals 13 (3) (2020), https://doi.org/10.3390/ph13030044.
[55] X. Jiang, S. Deng, L. Sun, J. Liu, N. Qi, Z. Chen, Pillared nickel-based metal-organic frameworks as electrode material with high electrochemical performance, J. Electroanal. Chem. 879 (2020) 114802, https://doi.org/10.3390/ph13030044.
[56] Esraa M. El-Fawal, H.M. Abd El Salam, Deposition of dyes on Cobalt-based metal-organic framework (Co-MOF) composites with promoted achievement photocatalytic degradation of an anionic dye (EBT) under visible light irradiation, Int. J. Environ. Anal. Chem. 103 (1) (2020) 1–17, https://doi.org/10.1080/03067319.2020.1853113.
[57] M.E. Bosch, A.R. Sánchez, F.S. Rojas, C.B. Ojeda, Analytical methodologies for the determination of cisplatin, J. Pharmaceut. Biomed. Anal. 47 (3) (2008) 451–459, https://doi.org/10.1016/j.jpba.2008.01.047.
[58] Mengwei Yuan, Rui Wang, Zemin Sun, Liu Lin, Han Yang, Huifeng Li, Caiyun Nan, Genban Sun, Shulan Ma, Morphology-controlled synthesis of Ni-MOFs with highly enhanced electrocatalytic performance for urea oxidation, Inorg. Chem. 58 (17) (2019) 11449–11457, https://doi.org/10.1021/acs.inorgchem.9b01124.
[59] W. Zhang, H. Yin, Z. Yu, X. Jia, J. Liang, G. Li, Y. Li, K. Wang, Facile synthesis of 4,4′-biphenyl dicarboxylic acid-based nickel metal-organic frameworks with a tunable pore size towards high-performance supercapacitors, Nanomaterials 12 (12) (2022) 2062, https://doi.org/10.3390/nano12122062.
[60] H. Zhao, H. Song, L. Chou, Nickel nanoparticles supported on MOF-5: synthesis and catalytic hydrogenation properties, Inorg. Chem. Commun. 15 (2011) 261–265, https://doi.org/10.1016/j.inoche.2011.10.040.
[61] J. Gascon, M.D. Hernandez-Alonso, A.R. Almeida, G.P.M. Van Klink, F. Kapteijn, G. Mul, Isoreticular MOFs as efficient photocatalysts with tunable band gap: an operando FTIR study of the photoinduced oxidation of propylene, ChemSusChem 1 (12) (2008) 981–983, https://doi.org/10.1002/cssc.200800203.
[62] H.P.N. Thi, H.D. Ninh, C.V. Tran, B.T. Le, S.V. Bhosale, D.D. La, Size-control and surface modification of flexible metal-organic framework MIL-53(Fe) by polyethyleneglycol for 5- fluorouracil anticancer drug delivery, ChemistrySelect 4 (8) (2019) 2333–2338, https://doi.org/10.1002/slct.201803887.
[63] S. Javanbakht, P. Nezhad-MoKhtari, A. Shaabani, N. Arsalani, M. Ghorbani, Incorporating Cu-based metal-organic framework/drug nanohybrids into gelatin microsphere for ibuprofen oral delivery, Mater. Sci. Eng., C 96 (2019) 302–309, https://doi.org/10.1016/j.msec.2018.11.028.
[64] N.J. Castellanos, Z. Martinez Rojas, H.A. Camargo, S. Biswas, G. Granados-Oliveros, Congo red decomposition by photocatalytic formation of hydroxyl radicals (OH) using titanium metal-organic frameworks, Transit. Met. Chem. 44 (2019) 77–87, https://doi.org/10.1007/s11243-018-0271-z.
[65] S. Javanbakht, M. Pooresmaeil, H. Hashemi, H. Namazi, Carboxymethylcellulose capsulated Cu-based metal-organic framework-drug nanohybrid as a pH-sensitive nanocomposite for ibuprofen oral delivery, Int. J. Biol. Macromol. 119 (2018) 588–596, https://doi.org/10.1016/j.ijbiomac.2018.07.181.
[66] X. Chen, R. Tong, Z. Shi, B. Yang, H. Liu, S. Ding, X. Wang, Q. Lei, J. Wu, W. Fang, MOF nanoparticles with encapsulated autophagy inhibitor in controlled drug delivery system for antitumor, ACS Appl. Mater. Interfaces 10 (3) (2018) 2328–2337, https://doi.org/10.1021/acsami.7b16522, 2018.
[67] Z. Liang, Z. Yang, H. Yuan, C. Wang, J. Qi, K. Liu, R. Cao, H. Zheng, A protein @metal-organic framework nanocomposite for Ph- triggered anticancer drug delivery, Dalton Trans. 47 (2018) 10223–10228, https://doi.org/10.1039/C8DT01789A.